

Light scattering by the Martian dust analog, palagonite, modeled with ellipsoids

S. Merikallio,^{1,*} T. Nousiainen,² M. Kahnert,^{3,4} and A.-M. Harri¹

¹Finnish Meteorological Institute, P.O. Box 503, 00101 Finland

²Department of Physics, University of Helsinki, P.O. Box 48, 00014 Finland

³Swedish Meteorological and Hydrological Institute, Folkborgsvägen 17, 60176 Norrköping,

Sweden//⁴Chalmers University of Technology, Department of Earth and Space Science,

41296 Gothenburg, Sweden

* Sini.Merikallio@fmi.fi

Abstract: We have investigated the suitability of the ellipsoidal model particles to mimic scattering by Martian dust particles by comparing simulations against laboratory data for palagonite, a Mars analog sample. By optimizing the shape distribution of ellipsoids, a very good match with a laboratory-measured scattering matrix was obtained. Even an equiprobable distribution of ellipsoids performed well. The asymmetry parameter and single-scattering albedo were found to depend on the assumed shape distribution as much as on the typical uncertainties associated with refractive indices and size, suggesting that shape is an important parameter that potentially influences remote retrievals of dust particle properties.

© 2013 Optical Society of America

OCIS codes: (010.1110) Aerosols; (290.1310) Atmospheric scattering; (290.5850) Scattering, particles; (290.5855) Scattering, polarisation.

References and links

1. Zh. M. Dlugach, O. I. Korablev, A. V. Morozhenko, V. I. Moroz, E. V. Petrova, and A. V. Rodin, "Physical properties of dust in the Martian atmosphere: Analysis of contradictions and possible ways of their resolution," *Solar Sys. Res.* **37**, 1–19 (2003).
2. O. Korablev, V. I. Moroz, E. V. Petrova, and A. V. Rodin, "Optical properties of dust and the opacity of the Martian atmosphere," *Adv. Space Res.* **35**(1), 21–30 (2005).
3. M. D. Smith, "Spacecraft observations of the Martian atmosphere," *Annu. Rev. Earth Planet. Sci.* **36**, 191–219 (2008).
4. M. J. Wolff, M. D. Smith, R. T. Clancy, N. Spanovich, B. A. Whitney, M. T. Lemmon, J. L. Lemmon, J. L. Bandfield, D. Bandfield, A. Ghosh, G. Landis, P. R. Christensen, J. F. Bell III, and S. W. Squyres, "Constraints on dust aerosols from the Mars Exploration Rovers using MGS overflights and Mini-TES," *J. Geophys. Res.* **111**, E12S17 (2006).
5. H. C. van de Hulst, *Light Scattering by Small Particles*, 2nd ed. (Dover Publications Inc., 1981).
6. J. E. Hansen and L. D. Travis, "Light scattering in planetary atmospheres," *Space Sci. Rev.* **16**, 527–610 (1974).
7. E. C. Laan, H. Volten, D. M. Stam, O. Muñoz, J. W. Hovenier, and T. L. Roush, "Scattering matrices and expansion coefficients of Martian analogue palagonite particles," *Icarus* **199**, 219–230 (2009).
8. O. Muñoz, O. Moreno, D. D. Dabrowska, H. Volten, and J. W. Hovenier, "The Amsterdam-Granada light scattering database," *J. Quant. Spectrosc. Radiat. Transfer* **113**, 565–574 (2012).
9. Z. Meng, P. Yang, G. W. Kattawar, L. Bi, K. N. Liou, and I. Laszlo, "Single-scattering properties of tri-axial ellipsoidal mineral dust aerosols: A database for application to radiative transfer calculations," *J. Aerosol Sci.* **41**, 501–512 (2010).
10. L. Bi, P. Yang, G. W. Kattawar, and R. Kahn, "Single-scattering properties of triaxial ellipsoidal particles for a size parameter range from the rayleigh to geometric-optics regimes," *Appl. Optics* **48**(1), 114–126 (2009).

11. S. Merikallio, H. Lindqvist, T. Nousiainen, and M. Kahnert, "Modelling light scattering by mineral dust using spheroids: assessment of applicability," *Atmos. Chem. Phys.* **11**(11), 5347–5363 (2011).
 12. I. Zelinka, V. Snasel, and A. Abraham, *Handbook of Optimization: From Classical to Modern Approach* (Springer, 2012).
 13. M. J. Wolff, R. T. Clancy, J. D. Goguen, M. C. Malin, and B. A. Cantor, "Ultraviolet dust aerosol properties as observed by Marci," *Icarus* **208**, 143–155 (2010).
 14. M. J. Wolff, M. D. Smith, R. T. Clancy, R. Arvidson, M. Kahre, F. Seelos IV, S. Murchie, and H. Savijärvi, "Wavelength dependence of dust aerosol single scattering albedo as observed by the Compact Reconnaissance Imaging Spectrometer," *J. Geophys. Res.* **114**, E2 (2009).
 15. F. M. Kahnert, J. J. Stamnes, and K. Stamnes, "Can simple particle shapes be used to model scalar optical properties of an ensemble of wavelength-sized particles with complex shapes?" *J. Opt. Soc. Am. A* **19**, 521–531 (2002).
 16. T. Nousiainen, M. Kahnert, and B. Veihelmann, "Light scattering modeling of small feldspar aerosol particles using polyhedral prisms and spheroids," *J. Quant. Spectrosc. Radiat. Transfer* **101**, 471–487 (2006).
 17. T. Nousiainen, E. Zubko, J. V. Niemi, K. Kupiainen, M. Lehtinen, K. Muinonen, and G. Videen, "Single-scattering modeling of thin, birefringent mineral dust flakes using the discrete-dipole approximation," *J. Geophys. Res.* **114**, D07207 (2009).
 18. T. Nousiainen, "Impact of particle shape on refractive-index dependence of scattering in resonance domain," *J. Quant. Spectrosc. Radiat. Transfer* **108**, 464–473 (2007).
 19. T. Nousiainen, K. Muinonen, and P. Räisänen, "Scattering of light by large Saharan dust particles in a modified ray optics approximation," *J. Geophys. Res.* **108**, 4025 (2003).
-

1. Introduction

Airborne dust is a ubiquitous feature of the otherwise optically thin Martian atmosphere, that can have substantial impact on the atmospheric thermal structure, near-surface climate, and global circulation. Absorption, emission, and scattering by airborne dust can also complicate the interpretation of remote sensing observations. While studies of these processes have been a major focus since the beginning of the space age, our understanding of the physical and optical properties of the dust is still inadequate. Shape and size distributions, surface roughness, mineralogical composition, internal structure of dust particles as well as their spatial distribution affect the radiative influence of the dust on the solar and thermal radiation field. All these quantities can in principle be retrieved from remote sensing observations. There have been several instruments flown in orbit and delivered to the surface of Mars whose measurements have given us some constraints on these properties (see e.g. [1–4]). However, these are only glimpses of the full range of unknowns. In the absence of direct measurements, the shapes of the Martian dust particles are particularly poorly constrained. In this study we aim to provide a usable model for Martian dust particles, to be used in applications of radiative transfer models.

Often in analysis of the radiance field, the possible variation with the shape is neglected and more weight is given for refractive index and particle size distribution. Here, we first consider whether the single-scattering characteristics of Martian dust analog particles, namely palagonite dust, could be modeled with ellipsoidally shaped model particles. We then investigate the effects of using different shape distributions of ellipsoids to calculate the single-scattering albedo and the asymmetry parameter. These two parameters are needed even in the simplest radiative transfer models.

The complex refractive index (m) of the palagonite sample is not known accurately so, for simulations, we tried several different refractive indices. The best fitting results were achieved with $\text{Re}(m) = 1.6$ and $\text{Im}(m) = 0.0005$. With this choice of m , the measured palagonite scattering matrix can be reproduced almost perfectly with ellipsoids. Moreover, even a very simple shape distribution, where all the shapes considered are present in equal quantities, performs well.

In Sect. 2 we briefly review single-scattering theory and introduce the main optical parameters that would be needed for radiative transfer calculations. In Sect. 3 we present the laboratory measurements of the optical parameters and particle size distributions of the palagonite sample. The methodology of fitting the observations with model results is explained in Sect. 4. We

also discuss how to constrain the refractive index of the palagonite particles. The results are presented and discussed in Sect. 5. Concluding remarks are given in Sect. 6.

2. Single-scattering theory

The scattering matrix describes the angular distribution of the scattered intensity and polarisation in the Stokes parameter description of electromagnetic fields. It is dependent on the particle's size, shape and composition as well as on the wavelength of the incident radiation. Assuming the scattering media to be an ensemble of randomly oriented particles and their mirror particles, the scattering matrix is left with only six independent non-zero matrix elements [5]:

$$P(\theta) = \begin{pmatrix} P_{11}(\theta) & P_{12}(\theta) & 0 & 0 \\ P_{12}(\theta) & P_{22}(\theta) & 0 & 0 \\ 0 & 0 & P_{33}(\theta) & P_{34}(\theta) \\ 0 & 0 & -P_{34}(\theta) & P_{44}(\theta) \end{pmatrix}, \quad (1)$$

where the scattering angle θ is the angle between the incident and the scattered light direction. The Stokes scattering matrix is normalized in such a way that its first element, the so called phase function P_{11} , integrates over the scattering angle θ as

$$\frac{1}{2} \int_0^\pi \sin(\theta) P_{11} d\theta = 1. \quad (2)$$

Integrating the phase function P_{11} over the phase angle θ , weighted with $\cos(\theta)$, yields a measure for the partitioning between scattering into the forward ($\theta < \pi/2$) and backward ($\theta > \pi/2$) hemispheres, the so called asymmetry parameter g :

$$g = \int_0^\pi P_{11} \cos(\theta) \sin(\theta) d\theta. \quad (3)$$

The asymmetry parameter g is an important parameter in radiative flux computations.

The scattering cross section, C_{sca} , is the total rate with which electromagnetic energy is scattered in relation to the incident radiative energy flux [5]. It depends on the size, shape and composition of the particle, as well as the wavelength of the incident radiation. Similarly, the absorption cross section, C_{abs} , is a measure for the rate of absorption of electromagnetic energy in relation to the incident electromagnetic energy flux. Together, the net effect of scattering and absorption is called extinction, with the extinction cross-section thus defined as:

$$C_{\text{ext}} = C_{\text{sca}} + C_{\text{abs}}. \quad (4)$$

The single-scattering albedo,

$$\omega = \frac{C_{\text{sca}}}{C_{\text{ext}}} = \frac{C_{\text{sca}}}{C_{\text{sca}} + C_{\text{abs}}}, \quad (5)$$

is a measure for the relative contribution of scattering to extinction. In the case of particle ensembles, the cross sections (C_{xx} , where 'xx' stands for 'abs', 'sca' or 'ext') are simply summed over all particles (shapes and sizes):

$$C_{\text{xx}} = \sum_i \eta_i \sum_r n_r C_{\text{xx}}(i, r), \quad (6)$$

where n_r and η_i are the distribution weights for the size and shape distribution bins, respectively. Their sums are normalized to unity. In case of the scattering matrix elements or the asymmetry

parameter, the ensemble-averaged quantities are additionally weighted by the corresponding C_{sca} of each particle, for example:

$$g = \frac{\sum_i \eta_i \sum_r n_r C_{\text{sca}}(r, i) g(r, i)}{\sum_i \eta_i \sum_r n_r C_{\text{sca}}(r, i)}. \quad (7)$$

A convenient way to characterize different size distributions is to use an effective radius and effective variance, because different size distributions with the same r_{eff} and v_{eff} scatter similarly [6]. The geometric cross-section-weighted mean radius is defined as

$$r_{\text{eff}} = \frac{\sum_r r \pi r^2 n(r)}{\sum_r \pi r^2 n(r)}, \quad (8)$$

where $n(r)$ is the number density; v_{eff} is a dimensionless geometric cross-section-weighted effective variance:

$$v_{\text{eff}} = \frac{\sum_r (r - r_{\text{eff}})^2 \pi r^2 n(r)}{r_{\text{eff}}^2 \sum_r \pi r^2 n(r)} \quad (9)$$

The definitions presented here are the discretized forms of the integral forms found in [6].

3. Measurements of palagonite dust

Light scattering measurements of palagonite particles were acquired from the Amsterdam Light Scattering Database [7, 8]. Palagonite is commonly used as a Martian dust analogue material and produces remarkably good agreement with phase functions derived from measurements [8]. The uneven and coarse nature of this palagonite sample gathered near the top of the Hawaii's Mauna Kea volcano can be seen in a Scanning Electron Microscope (SEM) picture in Fig. 1. Light scattering measurements were carried out at the wavelength of 632.8 nm and cover scattering angles $\theta = 3^\circ$ to 174° with steps of 5° from $\theta = 10^\circ$ to 170° , and with steps of 1° elsewhere. The measured scattering matrix, F' , is proportional to the phase matrix by an unknown normalization factor α such that $F' = \alpha F$. To facilitate comparisons with simulations, F' should be properly normalized. Due to the finite angle span and resolution of the measurements, however, the normalization integral Eq. (2) cannot be readily applied. One approach, which is also used here, is to fill the gaps in the measured F'_{11} by merging it with a simulated P_{11} . The forward peak (0° to 3°) was obtained by assuming the particles to be spherical, with an assumed refractive index, and by applying the measured size distribution of the palagonite particles in Mie computations. The values from 174° to 180° , on the other hand, were simply linearly extrapolated from the value measured at 173° . We could then apply Eq. (2) to normalize F'_{11} properly for comparisons with the simulated P_{11} .

The size distribution of the palagonite sample was measured with a laser diffraction method [7]. The measurements employ either Mie or Fraunhofer theory to retrieve the particle size distribution. Of these, the Mie-based size distribution (acquired from Olga Muñoz through personal communication) turned out to provide considerably better fits between the measured and simulated scattering matrices, and was therefore chosen as the size distribution of the palagonite sample in the following analysis. The estimated effective radius for this sample, based on the Mie theory, is quite high ($r_{\text{eff}} = 11.1 \mu\text{m}$), and differs considerably from that obtained with Fraunhofer theory ($r_{\text{eff}} = 4.5 \mu\text{m}$). The estimated complex refractive index m of the sample has been estimated to lie in between $1.5 + 0.001i$ and $1.5 + 0.0001i$.

A simple summation of root-mean-square errors was chosen for the purpose of comparing the measurements and the model. The cost function, E , for comparing the simulated quantity, $S(\theta)$, with the corresponding observed quantity, $O(\theta)$, can thus be expressed as:

$$E = \sum_{\theta} \rho_{\theta} / \pi [S(\theta) - O(\theta)]^2 / \sigma_{\theta}^2, \quad (10)$$

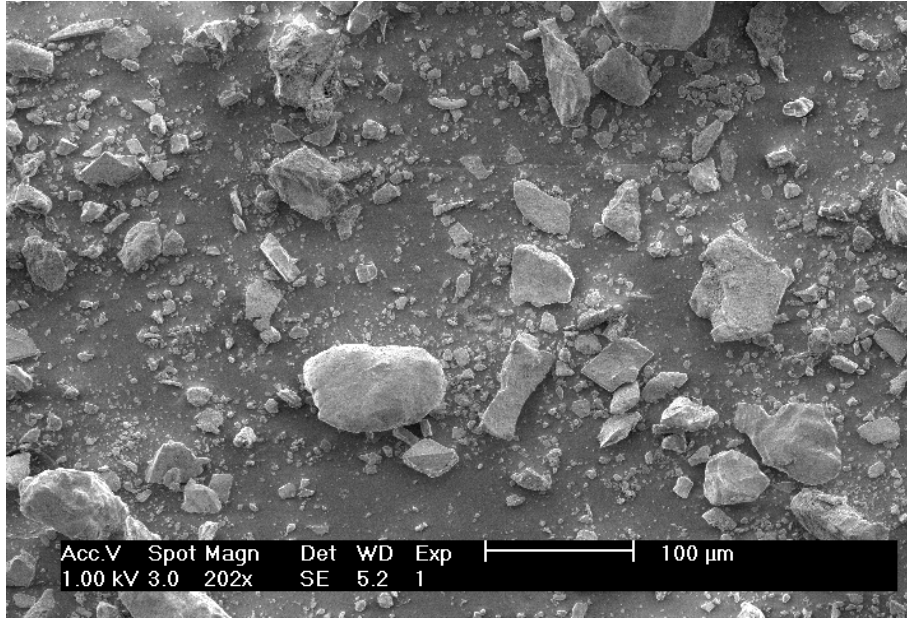


Fig. 1. Palagonite sample particles imaged with a Scanning Electron Microscope (SEM), courtesy of Olga Munõz.

where σ_θ is the measured standard deviation and ρ_θ is the width of the angular bin. For the phase function, $S(\theta) = \log(P_{11}(\theta))$ and $O(\theta) = \log(F_{11}(\theta))$, while for other scattering matrix elements $S(\theta) = P_{xy}(\theta)/P_{11}(\theta)$ and $O(\theta) = F_{xy}(\theta)/F_{11}(\theta)$, xy denoting the scattering matrix elements 12, 22, 33, 34 or 44.

4. Approach

We model the Martian dust particles using ellipsoids, a three dimensional form characterized in the Cartesian coordinate system by

$$x^2/a_e^2 + y^2/b_e^2 + z^2/c_e^2 = 1, \quad (11)$$

where a_e , b_e and c_e are the semi-axis of the ellipsoids. Using the nomenclature of [9] we adopt the order $c_e \geq b_e \geq a_e$. We do not suggest that the dust particles are ellipsoidal in shape, but rather that it may be possible to mimic the single-scattering properties of dust particle ensembles by suitable ensembles of ellipsoidal model particles. The ellipsoids have been shown to work well in describing the optical properties of terrestrial feldspar [10]. Spheroids, which are a subset of ellipsoids, have also been shown to work quite well for modeling scattering by terrestrial clays [11]. The scattering parameters for different ellipsoids are acquired from a database [9], which provides precalculated data for 42 different shapes with axis ratios ranging from 1 to 3.3. Database entries exist for 69 refractive indices with the real and imaginary parts of the refractive index ranging from $m_r \in [1.1, 2.1]$, and $m_i \in [0.0005i, 0.5i]$, respectively. There are 471 entries for size parameters $\chi = 2\pi c_e/\lambda$ ranging from 0.025 up to 1000. In order to obtain the model scattering matrix $P(\theta)$, all shapes were integrated over the measured size distribution as

$$P(\theta) = \frac{\sum_i \eta_i \sum_r n_r C_{sca}(r, i) P(\theta, r, i)}{\sum_i \eta_i \sum_r n_r C_{sca}(r, i)}, \quad (12)$$

where r is the particle size, i the index of shape, and $C_{\text{sca}}(r, i)$ the scattering cross-section of a particle with shape i and size r . The sum of shape-distribution weights, $\sum_i \eta_i$, equals unity.

The refractive index suggested in the literature for this palagonite sample [7, 8] ($m_r = 1.5$, $m_i \in [0.0001i, 0.001i]$) was found not to perform particularly well in the light-scattering simulations. Several alternative refractive indices were therefore tested. The one that finally turned out to provide the best fits was $m = 1.6 + 0.0005i$. Since this is not very far away from the expected value, we decided to use it in our analysis. The shape-distribution weights, η_i , were then varied and fitted in the search for the most suitable shape distribution model to describe the measured sample's radiative behavior. Tests were later also run with other values of m . These tests produced very similar best-fit shape distributions, but slightly larger value of the cost function.

5. Results

We first tested the suitability of the ellipsoidal model particles for simulating the single-scattering properties of palagonite dust (Section 5.1). After this (Section 5.2), we determined how our choice of the model particle shape affects the applications to real Martian dust.

5.1. Testing the model of ellipsoids

To test the performance of ellipsoids for Martian dust, we quantified how well it can reproduce the scattering matrix measured in a laboratory for the palagonite Martian analog sample. This is actually a stringent test, because the palagonite particles are clearly larger than those typically in the Martian atmosphere, and simple model particles can be expected to perform better for samples with smaller r_{eff} [11]. To quantify how well ellipsoids can reproduce the observations, we need to find weights for different ellipsoidal shapes such that their ensemble-averaged scattering properties optimally match the measurements. As the database contains data for 42 different ellipsoids, and we have measurements at 44 scattering-angles for each of the six scattering matrix elements, this is not a trivial task. Simple linear regression algorithms are not applicable, as no negative weights are allowed for the shapes. Non-linear fitting algorithms on the other hand, have difficulties when the degree of freedom is high, or else are exceedingly slow. To facilitate the fitting, we carried out lengthy brute-force runs where the shape distribution weights, η_i , were systematically varied through all possible combinations with 20% steps, to identify shapes that are not important for good fits and can therefore be excluded. From these runs it became obvious that the ellipsoids closest to the spherical shape were represented only very weakly or not at all in the best distributions. We thus proceeded in selecting a sub-set of 34 ellipsoids where all the nearly spherical shapes were omitted; the spherical case itself was included. These 34 shapes include 6 prolate and 6 oblate spheroids and the sphere. We then applied a standard Monte Carlo simulated annealing algorithm to find the best-fit shape distributions [12]. In this method, we start with a random shape distribution and proceed in modifying this distribution with random variations. If the new distribution reduces the cost function, we accept that as our new starting distribution and slowly, with millions of iterations, move towards smaller cost function values. In order to provide a means for the algorithm to rise from local minima, the algorithm now and then accept steps that take the cost function to a higher value. This acceptance probability is dependent on the simulation time, such that in the beginning the probability of acceptance is high (i.e. the system is 'hot') whereas towards the end only very few of the cost function increasing steps are accepted (i.e. the system 'cools'; hence the name 'simulated annealing'). This method was found to produce very good fits for this subset of 34 shapes in quite a reasonable time.

In Fig. 2, a comparison between the measurements and the separately fitted model matrix elements is shown. The measurements are plotted with red error bars and the best-fit ellip-

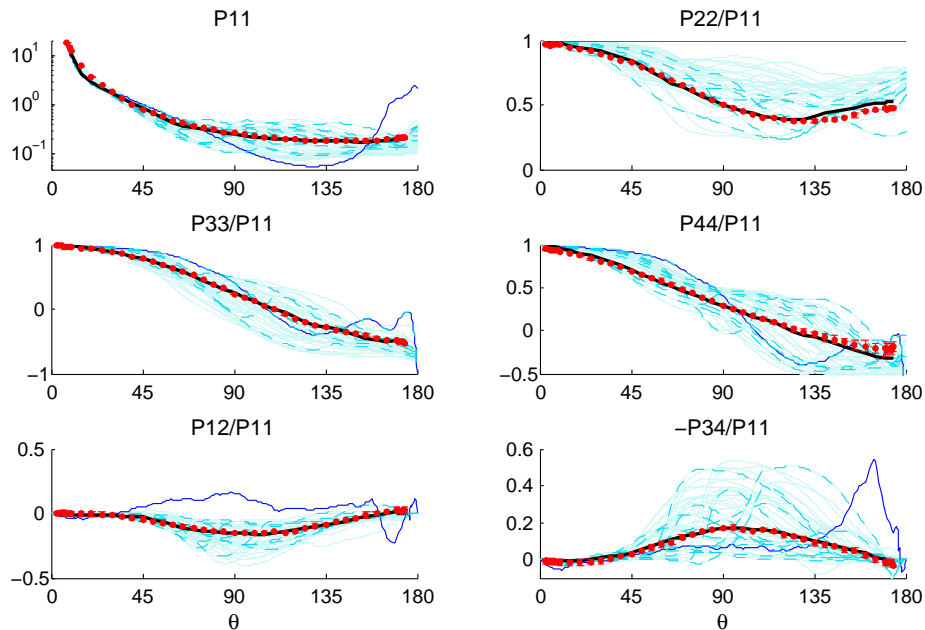


Fig. 2. Comparison of measured (red error bars) and modeled scattering matrix elements for the best-fit shape distribution (black line) as well as individual ellipsoids (turquoise lines, with an exception of the Mie-shape being plotted in blue). The shapes that are represented with more than one percent in the best-fit shape distribution are marked with thicker and dashed turquoise line. The only obvious room for improvement of the fitting resides in the tail of P_{22} and P_{44} , and in the forward scattering angles of the phase matrix P_{11} .

solid model outcomes are plotted in black lines closely following, and often overlapping, the measurements. Scattering matrix elements of individual ellipsoidal shapes are shown in the background in light turquoise, the exception among those being the sphere, which has been plotted in blue. Those individual ellipsoidal curves that have more than 1% weight in the best-fit distribution have been plotted with a dashed line of slightly darker color. It can be seen that the ellipsoids cover a large percentage of possible matrix element values, including those measured for the palagonite dust. Consequently, it is not surprising that very good fits to the measured matrix elements are obtained. As perfect spheres do not depolarize, the blue curve for element P_{22}/P_{11} is uniformly equal to unity. The model is seen to wander noticeably outside the measured values only around $\theta = 15^\circ$ for P_{11} , and in forward and backward scattering parts of P_{22}/P_{11} and P_{44}/P_{11} .

Unfortunately, the palagonite sample has been measured only at one wavelength. The consistency of the method, that is, are the fits acquired by using the same shape distribution good on multiple wavelengths, cannot be evaluated that way. We thus performed the fits separately for each measured scattering matrix element to see if they are all best reproduced using similar shape distributions. These distributions are shown in Fig. 3, individual weights being directly proportional to the sizes of the black circles. The red crosses, on the other hand, show the shape distribution acquired when the whole matrix is fitted simultaneously. It was disappointing, but not surprising, to find that the shape distributions that fit the individual scattering matrix elements vary significantly among the individual elements. It can be expected that similar vari-

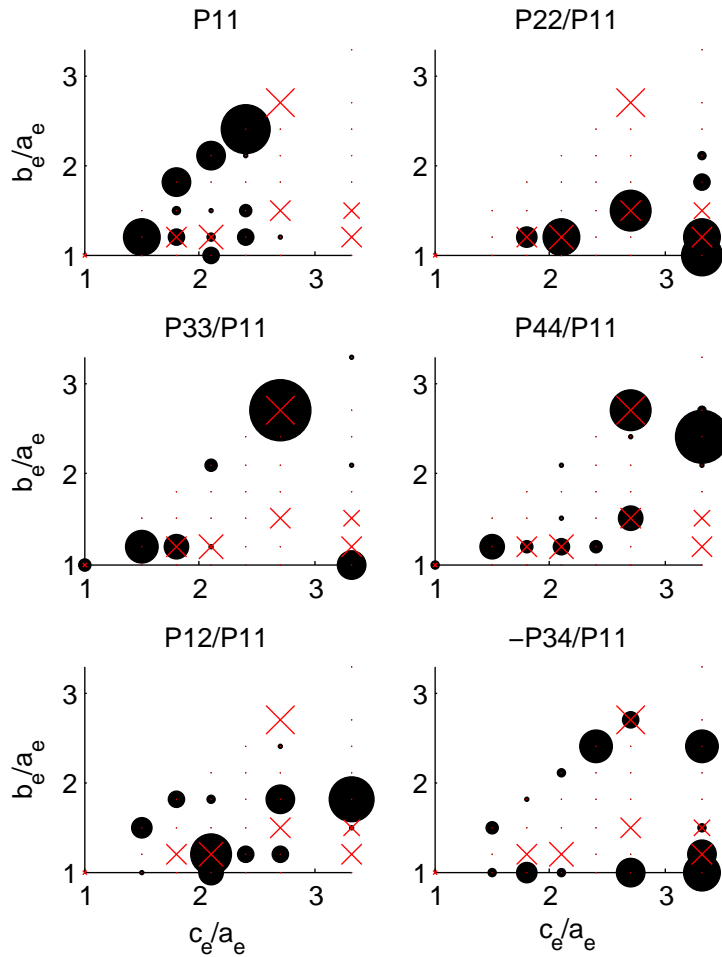


Fig. 3. Shape distribution weights that optimally reproduce the scattering matrix element in question (black balls) and for optimally fitting the whole matrix (red crosses), as a function of the axis ratios of the two largest axis, c_e and b_e , to the shortest axis, a_e . The size of the marker is directly proportional to the weight of the corresponding shape. Oblate spheroids are found on the diagonal whilst the prolate spheroids reside on the x-axis.

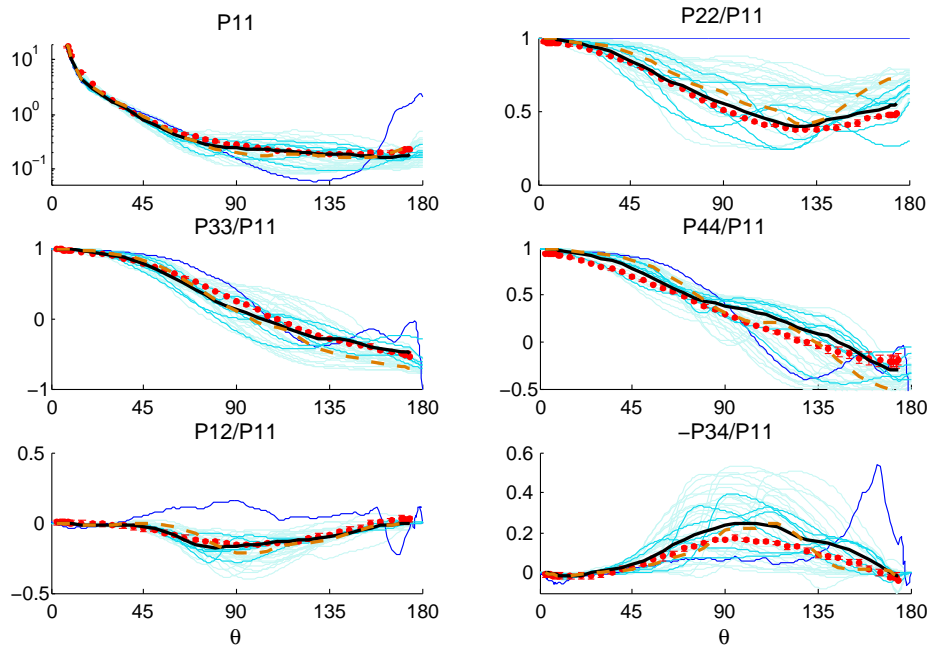


Fig. 4. Same as Fig. 2, but for the model (black line) that has been acquired by fitting all matrix elements simultaneously. The corresponding best fit obtained using only spheroids have been added for comparison (dashed orange line).

ability would be observed between different wavelengths as well. Whilst the oblates (dots on the diagonal) are major constituents in fitting the P_{11} , prolate-like shapes (x-axis) dominate P_{22} and are also well represented in other polarization elements. Curiously though, pure prolates are absent when the whole scattering matrix is fitted simultaneously, replaced by slightly squashed prolates.

When a good fit is sought for the whole of the scattering matrix simultaneously, the fitting errors understandably increase noticeably, as can be seen by comparing Figs. 2 and 4. Even then, however, the fits are very encouraging and the superiority of the ellipsoid model compared to the traditionally used Mie scattering results for equivalent spheres can be settled with a glance. The best-fit shape distribution for the overall scattering matrix is presented in Fig. 3 with the red crosses. Again, the prolate-like shapes are prevalent, with only one oblate-like shape prominent. Tempted as one might be to suggest a pure prolate distribution, the idea is contradicted by the complete absence in pure prolate forms in the overall best-fit shape distribution.

To compare the performance of the ellipsoid model with that based on spheroids (e.g. [11]), Fig. 4 also shows the corresponding best fit of the palagonite sample based on spheroids (dashed orange line). Clearly, ellipsoids provide a better overall match for the measured matrix, even though for one scattering element, P_{34}/P_{11} , spheroids actually match the measurements closer. The root mean square error for the best spheroids fit is 3.6 times best-fit ellipsoids; for individual scattering matrix elements, the errors are 3.2, 5.5, 2.4, 1.3, 3.6 and 0.7 times those of ellipsoid fits for $\log(P_{11})$, P_{22}/P_{11} , P_{33}/P_{11} , P_{44}/P_{11} , P_{12}/P_{11} and P_{34}/P_{11} respectively. As expected, the difference in favour of ellipsoids is most marked for P_{22}/P_{11} , presumably because ellipsoids are less symmetric and thus better represent the real shapes of the palagonite particles.

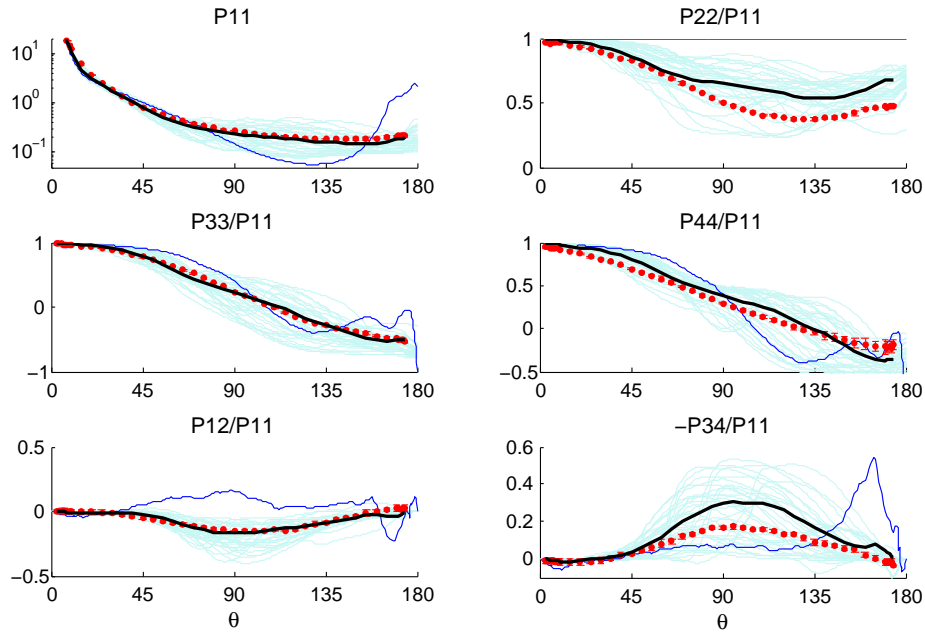


Fig. 5. The fits acquired by the equiprobable distribution. The symbols and colors are the same as in Fig. 4.

Considering that the best fits for each scattering matrix element are achieved with different shape distributions of ellipsoids, it is difficult to suggest any shape distribution to be particularly suitable for Martian dust. In Fig. 5 we show that even a shape distribution where the weights of all of the model ellipsoids have been equalized, a so-called equiprobable distribution, produces surprisingly accurate fits for P_{11} , P_{12}/P_{11} , and P_{33}/P_{11} elements, making it a good and simple first guess shape distribution.

5.2. Application to Martian dust

The results obtained with the palagonite sample do not strongly suggest any specific shape distribution of ellipsoids to be representative of Martian dust. It might be possible to retrieve such a distribution using remote sensing data together with a suitably parameterized shape distribution function (small number of free parameters). In the absence of such data, we conduct here a sensitivity study instead, aimed at quantifying how and how much the simulated Martian dust single-scattering properties can be expected to depend on the choice of the shape distribution. We also compare the outcome to those arising from varying the size distribution and the imaginary part of the refractive index.

For simplicity, we only consider asymmetry parameter, g , and single-scattering albedo, ω , here. Particle sizes are assumed to follow the Gamma distribution, defined as

$$n(r) = c \cdot r^{\frac{1-3v_{\text{eff}}}{v_{\text{eff}}}} e^{-\frac{r}{v_{\text{eff}}}} \quad (13)$$

where r_{eff} and v_{eff} are the effective radius and variance defined in Eqs.(8) and (9). The constant c is set by normalization by demanding that the total particle number $N = \int_r n(r) dr$. For r_{eff} and v_{eff} , we adopt the same values as in recent studies [13, 14]: $r_{\text{eff}} = 1.4, 1.6$ and $1.8 \mu\text{m}$ and

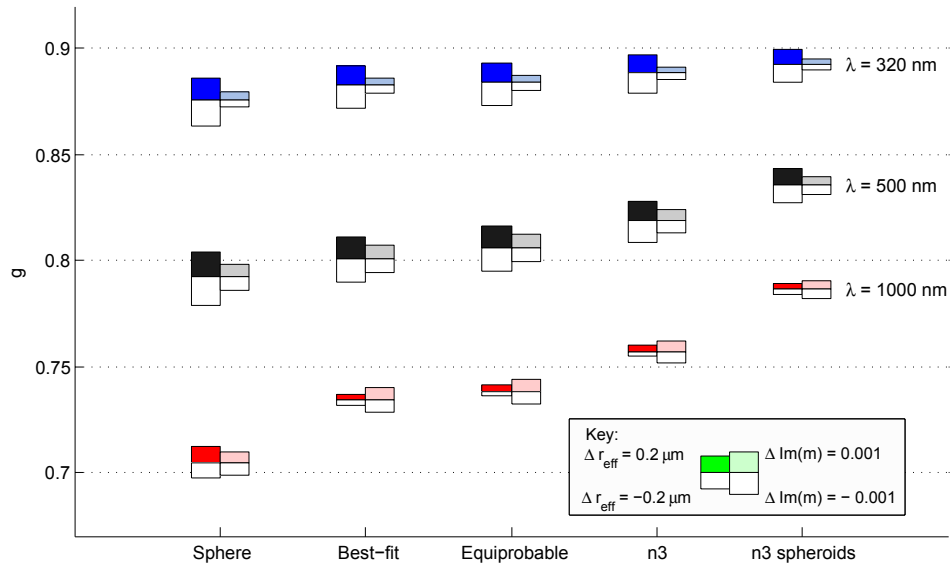


Fig. 6. The asymmetry parameters obtained with various shape and size distributions, refractive indices and at different wavelengths λ . The different shape distributions are shown on the x-axis, the middle three denoting different cases employing all 34 ellipsoids considered. Different wavelengths are denoted with different colors: 320 nm (blue), 500 nm (black), and 1000 nm (red). The boxes show results for different size distributions (left) and imaginary parts of the refractive index (right) so that the top of the box corresponds to the highest, and the bottom to the lowest value used, the midline presenting the value for the default case: for r_{eff} this is $1.6 \mu\text{m}$ while for $\text{Im}(m)$ it is wavelength-dependent and taken from Table 1.

$v_{\text{eff}} = 0.3$. We consider three wavelengths, from UV to near IR, namely 320, 500 and 1000 nm. As the refractive indices, we use the values recently retrieved for Martian dust - they are tabulated in Table 1.

Values for the imaginary part of the refractive index depend on the particle size distribution assumed when retrieving them, but for simplicity, and to facilitate comparisons, we use those values obtained by assuming $r_{\text{eff}} = 1.6 \mu\text{m}$ even when r_{eff} is varied. This way, impacts from size and refractive index can be separated and compared against each other. Also for simplicity, the real part of the refractive index was set to 1.5. The scattering properties corresponding to the different imaginary indices were interpolated from the database using splines.

Figure 6 shows the asymmetry parameters acquired for three different ellipsoidal distribu-

Table 1. Assumed complex refractive index, m , for Martian dust at the three wavelengths considered.

λ	m	source
$\lambda_{\text{UV}} = 320 \text{ nm}$	$1.493 + 0.0146i$	[13]
$\lambda_{\text{vis}} = 500 \text{ nm}$	$1.50 + 0.0065i$	[14]
$\lambda_{\text{IR}} = 1000 \text{ nm}$	$1.495 + 0.002i$	[14]

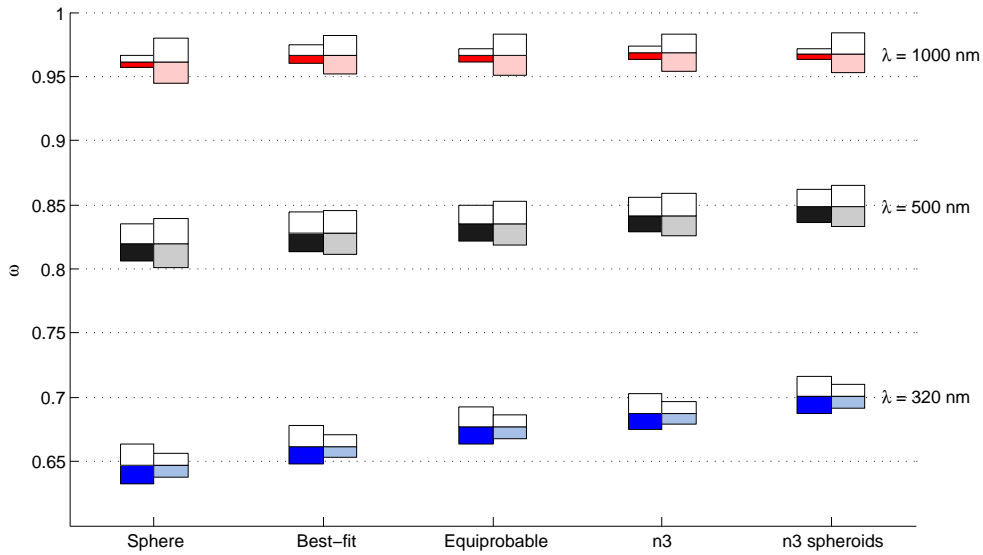


Fig. 7. The single-scattering albedo compared for various shape distributions, size distributions and refractive indices. The color coding for the boxes is the same as in Fig. 6 and the same legend can be applied. As in Fig. 6, the effects of variations of $\Delta r_{\text{eff}} = \pm 0.2 \mu\text{m}$ and $\Delta \text{Im}(m) = \pm 0.2$ are shown in colors towards the increasing value - note that here an increase in r_{eff} or $\text{Im}(m)$ results in a decrease in ω .

tions employing all the ellipsoids considered, and additionally the special cases of spheres and $n = 3$, aka. n3, distribution of spheroids. In the spheroid n3 distribution, which has in our previous study been suggested to be a reasonable choice for various clay minerals [11], the spheroidal shapes are weighted such that the $\eta_i \propto |\xi|^n$, $n = 3$, where ξ is the so-called shape parameter that quantifies the deviation of the particle shape from the sphere [15]. The shape parameter for spheroids is determined as a function of the aspect ratio $\varepsilon = a/b$, where b is the main rotational symmetry axis, and a the axis perpendicular to it, as [16]:

$$\xi = \begin{cases} \varepsilon - 1 & \varepsilon > 1 \quad (\text{oblate, } b < a) \\ 1 - 1/\varepsilon & \varepsilon < 1 \quad (\text{prolate, } b > a) \\ 0 & \varepsilon = 1 \quad (\text{sphere, } b = a) \end{cases} \quad (14)$$

Now, analogously to Eq. (14), we can define a shape parameter for ellipsoids, ξ_e , as the pythagorean summation of the individual shape parameters for the ratios of the largest, c_e , and smallest, a_e , axes on the middle axis (the middle axis aspect ratio is $1 - b_e/b_e = 0$, and thus does not contribute):

$$\xi_e = \sqrt{(1 - b_e/c_e)^2 + (1 - a_e/b_e)^2}, \quad (15)$$

where the largest axis has been treated prolate-like, and the smallest axis oblate like following Eq. (14). This quantifies the deviation from the spherical shape for the ellipsoids, treating both the prolate and oblate forms equally. The added beauty in this presentation reveals itself when one notes that, due to differing definitions of $\{a, b\}$ compared to $\{a_e, b_e, c_e\}$ (later are in order of length, whilst b always signifies the main rotational axis of the spheroid, and is smaller than a for oblates), for prolate spheroids ($a_e = b_e \leq c_e$), $a_e = b_e = a$ and $c_e = b$, which leads to $\xi_e = \xi$ (from Eq. (14)). Similarly, for oblate spheroids ($a_e \leq b_e = c_e$), $a_e = b$ and $b_e = c_e = a$

leading to $\xi_e = |\xi|$. For ellipsoid $n=3$ distribution, ξ_e^n shape distribution is adapted, such that the $\eta_i \propto \xi_e^n$, $n = 3$. Shown are also the results for the equiprobable and the best-fit shape distributions (red crosses in Fig. 3).

For each shape distribution case, three groups of boxes are shown, which are color-coded to indicate the wavelength (red for $\lambda = 1 \mu\text{m}$, black for $\lambda = 500 \text{ nm}$ and highest up the blue for $\lambda = 320 \text{ nm}$). Results for three different values of r_{eff} and $\text{Im}(m)$ are also shown, corresponding to the changes of r_{eff} and $\text{Im}(m)$ in the range of typical uncertainties: the midline of each cluster of four boxes is calculated with $r_{\text{eff}} = 1.6 \mu\text{m}$ and the imaginary refractive index corresponding to the wavelength as indicated. The leftmost boxes of each cluster are associated with the changing size distribution r_{eff} , while the rightmost, lighter colored boxes associate with the changing $\text{Im}(m)$. The colored box always shows the effect of increment in the parameter depicted, while the white shows the effect of decreasing the value; e.g., the effect of varying the size distribution r_{eff} with $\pm 0.2 \mu\text{m}$ is shown in Fig. 6 in the height of the leftmost boxes such that the upper edge of the colored box indicates increment by $0.2 \mu\text{m}$ (resulting in $r_{\text{eff}} = 1.8 \mu\text{m}$), while the lower border of the white box shows the value of g with $r_{\text{eff}} = 1.4 \mu\text{m}$. Likewise, the right side of box groups indicates the corresponding effect on g from varying $\text{Im}(m)$ with ± 0.001 . A similar plot is provided for the single-scattering albedo, ω , in Fig. 7. We see that, as expected, the behaviour of ω with respect to the particle size as well as with respect to the wavelength and refractive index is reversed when compared with the behaviour of the g .

When compared with the spheroid-only $n = 3$ distribution, using full range of ellipsoids gives values of g and ω somewhat closer to those obtained with the other shape distributions considered. This suggests that the value for g increases with elongation of the scatterer, which is consistent with high reported values of g for very thin flakes by [17]. One also observes that g increases with the r_{eff} and decreases with the wavelength. Not surprisingly, the sphere gives results in the one extreme, in this case lower g and slightly lower ω than for the others shapes.

It is quite encouraging to see that the equiprobable shape distribution produces values very close to the best-fit solution, suggesting that it might indeed be a good first guess shape distribution of ellipsoids to be used for real Martian dust. Also, for $g(\lambda_{\text{IR}})$, the absolute difference between the Mie-solution and the best-fit solution is only slightly larger than that between the best-fit and the equiprobable distributions - for other cases, the difference is even smaller. In contrast, it is not surprising that the $n = 3$ spheroid distribution, previously used for terrestrial dust (see [11]), deviates most from the Mie solutions, because they represent the most aspherical particle ensemble considered here, and give large weight to very elongated shapes known to have unusually high asymmetry parameters (see [17]). It thus seems that, at least for the cases studied, g increases monotonically with increasing departure from spherical shape, while the single-scattering albedo is almost insensitive to shape. It should be noted however, that this relation may not be universal but rather depends on the characteristics of the particle ensemble in question, namely on particle sizes [18].

The differences in g between different shape distributions decrease with decreasing wavelength. This is most likely due to the associated increases in the imaginary part of the refractive index and in the size parameter, which both act to strengthen absorption that dampen the internal fields and thus the shape-dependent interference. Accordingly, scattering becomes more dominated by surface reflection which, in contrast, is identical for all convex shapes when averaged over all particle orientations [5, 19]. Together these effects lead to shape playing a smaller role for higher imaginary refractive indices when the variation of g is considered [18]. For ω , the situation is the opposite, there being almost no change with the shape for the λ_{IR} .

Figure 6 shows the relative sensitivity of the asymmetry parameter to the changes of shape compared to those due to size and $\text{Im}(m)$ at different λ . For λ_{IR} , the shape is clearly more influential than the size, while at λ_{UV} , shape influences g only modestly. At λ_{vis} size and shape

seem to have equal effects. For the single-scattering albedo, ω (Fig. 7), the dependencies are reversed: the IR side, λ_{IR} , is very insensitive to both size and shape, whilst UV, λ_{UV} , manifests the largest sensitivity to the particle shape distribution. It can be noted that at λ_{IR} and λ_{vis} , the changes in $\text{Im}(m)$ dominate. In radiative transfer applications, however, both g and ω are needed, so the effect of shape should not be disregarded at any λ .

6. Concluding remarks

Suitability of the ellipsoidal model particles to mimic scattering by Martian dust particles was studied by comparing simulations against laboratory data for palagonite. We embarked on this study at two fronts. On the one hand, we investigated how well the single scattering characteristics of the palagonite, a commonly used Martian dust analog material, could be reproduced by using ellipsoids. On the other hand, we performed sensitivity studies to quantify how much different assumptions about the imaginary part of the refractive index, size distribution and particle shapes affect the calculated optical properties.

Our results show that the ellipsoidal model particles perform well in reproducing the measured scattering matrix elements of the palagonite Mars analog dust. The optimal shape distribution, however, differs considerably and seemingly arbitrarily among the individual scattering matrix elements. This implies that the ellipsoidal model is not entirely consistent and makes it difficult to suggest an ideal shape distribution to be used for palagonite particles and further to Martian dust.

A simple equiprobable distribution of the ellipsoids produces well-matching scattering parameters, which makes it a reasonable first approximation for modelling Martian dust optical properties. Moreover, when comparison is made between the single-scattering albedo, ω , and the asymmetry parameter, g , acquired with parameters representative of the real Martian dust, the equiprobable ellipsoid distribution performs very similarly to the best-fit shape distribution that optimally reproduced the laboratory-measured scattering matrix of the palagonite analog.

Variations in shape seem to impact g and ω roughly as much as variations in the size distribution and the imaginary part of the refractive index, when applied within reasonable bounds, except at the infrared wavelength, where ω is almost insensitive to shape. Our results thus indicate that it is often possible to acquire the same values for g and ω from the models by tuning the shape of the scatterers rather than sizes or refractive indices. Previous investigations have mostly neglected the impact of shape of the scattering particles when retrieving the dust particle properties. This omission may have led to uncertainties in the retrieved characteristics of the Martian dust particles, such as their sizes and refractive indices. To quantify these uncertainties, we plan to revisit some of the previous inversions using ellipsoids with varying shape distributions.

Acknowledgments

We thank Olga Muñoz and Hester Volten for making their measurement data publicly available and Zhaokai Meng for the use of his ellipsoid database, both of which were vital to this study. We also thank David Crisp and Olga Muñoz for their insightful comments on the manuscript. Authors are thankful for the Finnish Academy grants (contracts 1241212312, 131723 and 125180). M. Kahnert acknowledges funding from the Swedish Research Council (project 621-2011-3346).